Supplemental Material

Supplementary information

Improved estimates of changes in upper ocean salinity and the hydrological cycle

Lijing Cheng[1,2,6*], Kevin E. Trenberth[3], Nicolas Gruber[4], John P. Abraham[5], John T. Fasullo[3], Guancheng Li[1,6], Michael E. Mann[7], Xuanming Zhao[1,6], Jiang Zhu[1,2,6]

[1] International Center for Climate and Environment Sciences, Institute of Atmospheric Physics, Chinese Academy of Sciences, Beijing, China, 100029.

[2] Center for Ocean Mega-Science, Chinese Academy of Sciences, Qingdao, China, 266071.

[3] National Center for Atmospheric Research, PO Box 3000, Boulder, CO 80307, USA.

[4] Environmental Physics Group, Institute of Biogeochemistry and Pollutant Dynamics, ETH Zurich, 8092 Zürich, Switzerland.

[5] University of St. Thomas, School of Engineering,2115 Summit Ave., St Paul, MN 55105, USA.

[6] University of Chinese Academy of Sciences, Beijing, China.

[7] Department of Meteorology and Atmospheric Science, Pennsylvania State University, University Park, PA 16802, USA.

***** Correspondence to: Lijing Cheng: chenglij@mail.iap.ac.cn

1. Sampling error at different vertical layers

Figure 5 in the main manuscript already shows the global and basin 0-2000m mean sampling error compared with the reconstructed salinity changes. Here we analyze the sampling errors for different vertical layers (0-500m, 500-1000m, 1000-1500m, and 1500-2000m) separately in Figs. S2-S5. The observations tend to get scarcer with depth (Fig. 1), limiting the reliability of the reconstructions with regard to deep ocean changes. But the signals are much more persistent in the deep ocean and the short-term variability is much larger near the surface.

In the upper ocean between 0-500m (Fig. S2), the reconstructed global mean salinity reveals negative anomalies before 1990s and an upward trend since the 1990s, but the overall long-term trend since 1960 is insignificant (at the 90% confidence level). Meanwhile, there is a systematic negative sampling error before 2003 (~0.0025 g kg^{-1}), which is close to the reconstructed negative salinity anomalies from 1960s to 1990s. Therefore, the global 0-500m salinity changes are yet to be identified on both decadal/multi-decadal and inter-annual scales before 2005, with a signal-to-noise ratio (SNR) ~1 (Fig. S2g). However, the sampling errors are around zero since 2005 due to the establishment of Argo network, and the SNR is more than 2 for both decadal and inter-annual variability, suggesting a reliable reconstruction during the Argo period (Fig. S2g, h).

Although the signal-to-noise ratio is poor for global values in the upper ocean in part because the signal is weak, it is much better for regional patterns and at depth. The basin-scale freshening trend within the upper 500m in the Pacific Ocean (Fig. S2d), and the salting trend in the Atlantic Ocean (Fig. S2b) are both highly detectable from sampling uncertainty (SNR>>2 since 1960 for decadal/multi-decadal variability in Fig. S2g). In the North Indian Ocean, strong decadal fluctuations, which are larger than the sampling uncertainty (Fig. S2c, g), occur. For all six basins, the inter-annual variability is more detectable after 2005 than before (SNR>2, Fig. S2h).

For the 500-1000m layer (Fig. S3), the global mean salinity signals (Fig. S3a) are highly detectable (SNR ~3 before 2005 and ~5 after 2005) from the sampling errors on decadal/multi-decadal scales (Fig. S3g). The global 500-1000m freshening is dominated by the freshening trends (SNR>2) in the Pacific, South Indian and Southern oceans, mainly because of the transport of freshening low-salinity intermediate waters at higher latitudes (>30^{o}N and <30^{o}S) in the Southern Ocean and North Pacific Ocean (also see the vertical section of salinity change in Fig. 6). The SNR for the inter-annual variability is more than 2

only for the Atlantic and North Indian Ocean after 2005 because, in the other basins, the inter-annual fluctuations are much smaller for the 500-1000m layer compared to that in the 0-500m layer.

For the 1000-1500m and 1500-2000m layers (Figs. S4-5), the global mean changes show similar (although much weaker) fluctuations associated with the changes in the Atlantic Ocean (Fig. S4b, S5b), where considerable decadal-scale salinity variations occur. This reveals the active deep ocean formation of salinity anomalies in the North Atlantic Ocean (*21*). Below 1000m, only the Atlantic shows SNR>2 on both decadal/multi-decadal and inter-annual scales. The Pacific freshening is marginally significant in the 1000-1500m layer (SNR~2, Fig. S4g). All other basins show very small long-term and inter-annual salinity variations that are comparable with the sampling uncertainty (Fig. S4g, h, 5 g, h). There is an upward salinity trend for the 500-1000m layer in the Atlantic Ocean, superimposed on a decadal fluctuation, mainly revealing the impact of the Mediterranean Sea saltier water and its intrusion into the Atlantic Ocean (also see the vertical section of salinity change in Fig. 6).

2. SC1000 and SC2000-q indices

The two subsurface indices SC2000-q and SC1000 yield similar long-term increase as SC0 and SC2000, implying a 3.1±0.3% and 5.4±0.6% increase of salinity-contrast from 1960-2017, respectively (Table 1, Fig. S8). And, it takes ~12 and ~11 years for SC1000 and SC2000-q to emerge, indicating that they are less strongly affected by short-term fluctuations (i.e. inter-annual variability) than surface metric SC0.

For SC2000-q and SC1000, the median trends of both CMIP5-Hist and current results exceed the 2σ natural range (>95% confidence level). Six out of seven independent salinity reconstruction products show a SC2000-q and SC1000 increase in the past decades that exceeds the 2σ natural range (Figs. S8c-d). For the two indexes, the difference between model and observation is larger than SC2000 and SC0, probably related to the model biases in simulating vertical salinity structures, which is evidence in previous analysis on subsurface temperature changes (Cheng et al. 2016; Bilbao et al. 2019). The model errors need in-depth investigations in the future.

If we derive the E-P change by multiplying observed SC2000-q or SC1000 changes with the model-derived slopes for 1960-2030, the observed changes in the salinity-contrast metric, i.e., 3.1±0.3% SC2000-q and 5.4±0.6% SC1000 over the period 1960-2017 result in a change in the E-P contrast of 7.4 ±4.0%, 6.7 ±5.9%. The slopes derived from CMIP5-Hist

within 1960-2005 lead to a weaker but still positive E-P contrast (2.8±2.9% for SC2000-q, 2.4±2.6% for SC1000). Furthermore, by using the observed land/ocean surface warming of 0.88±0.11 K for 1960-2017 and adopting the 1960-2005 salinity/E-P correlation, we can infer a water cycle amplification of 2.8±3.0% K^{-1} for SC1000 and 3.2±3.4% K^{-1} for SC2000-q.

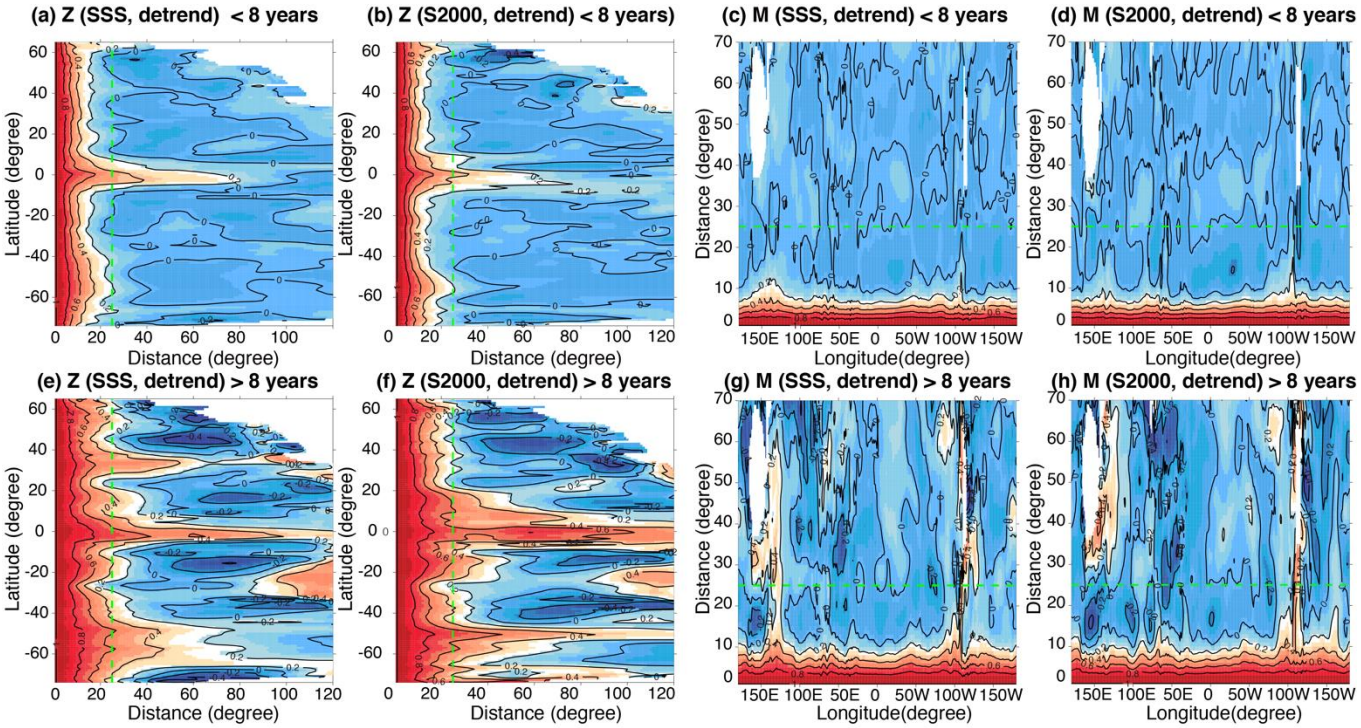

Supplementary Fig. S1. Zonal-mean (a, b, e, f) and Meridional-mean (c, d, g, h) correlation as a function of distance for SSS (a, e, c, g) and S2000 (b, f, d, h) respectively. The calculation is based on historical simulation within 1960-2017 (RCP4.5 from 2006-2017) from Goddard Institute for Space Studies (GISS-E2-H), but using other models show similar results. The mean seasonal cycle and a linear trend have been removed when calculating the correlation. The upper panels show the results for high-frequency variability (<8 years) and the lower panels shows the decadal/multi-decadal variability (>8 years).

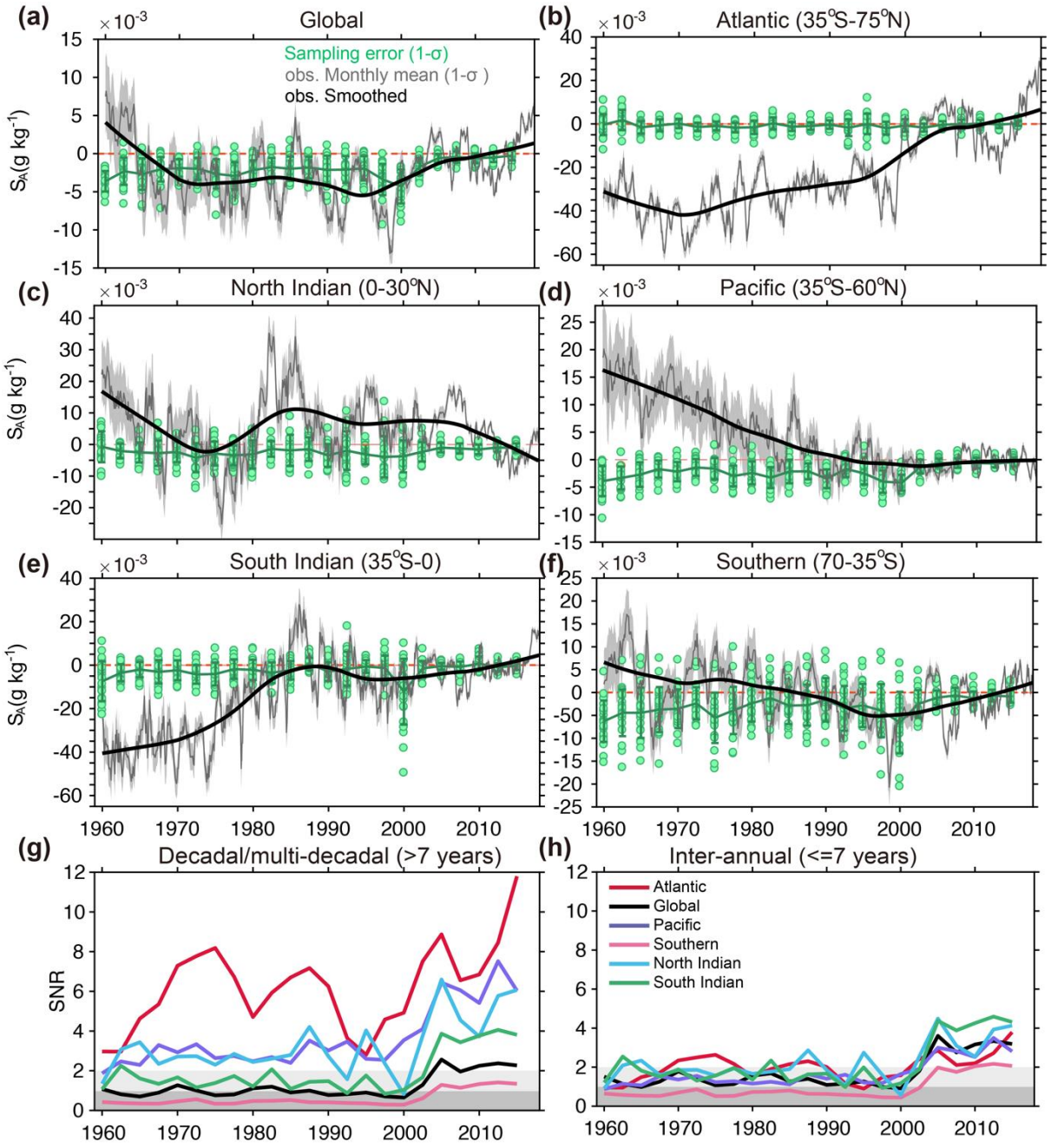

Supplementary Fig. S2. Global and basin averaged sampling error compared with reconstructed salinity change within 0- 500m. Dots represent the sampling errors corresponding to 22 different "Truth" fields, accompanied with mean in lines and 1 standard deviation error bars. The grey line is the monthly salinity anomaly time series from 1960 to 2017 based on the current analysis (with grey shading showing 1σ confidence interval, calculated by one standard deviation of the ensemble members). The dark black line is the time series after applying a LOWESS (Locally Weighted Scatterplot Smoothing) with a span width of 240 months. (a) Global, (b) Atlantic, (c) North Indian, (d) Pacific, (e) South Indian, (f) Southern oceans. (g) and (h) show the signal-to-noise ratio (SNR) for salinity change on

two different time scales: decadal/multi-decadal (>7 years) and inter-annual scales (<7 years). SNRs for the global time series and different basins are provided. SNR<1 and <2 are shaded.

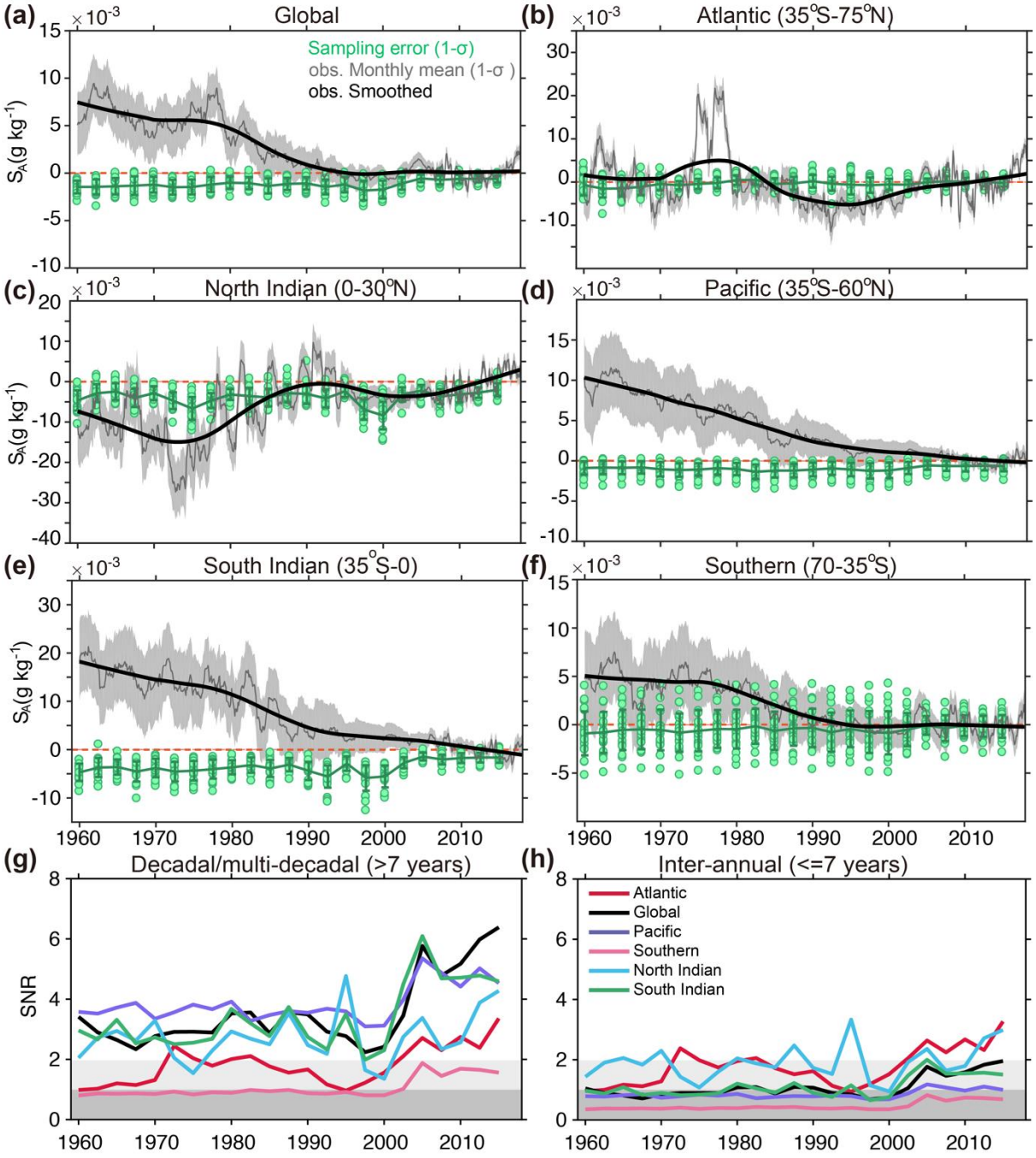

Supplementary Fig. S3. As for Fig. S2 but for 500-1000m.

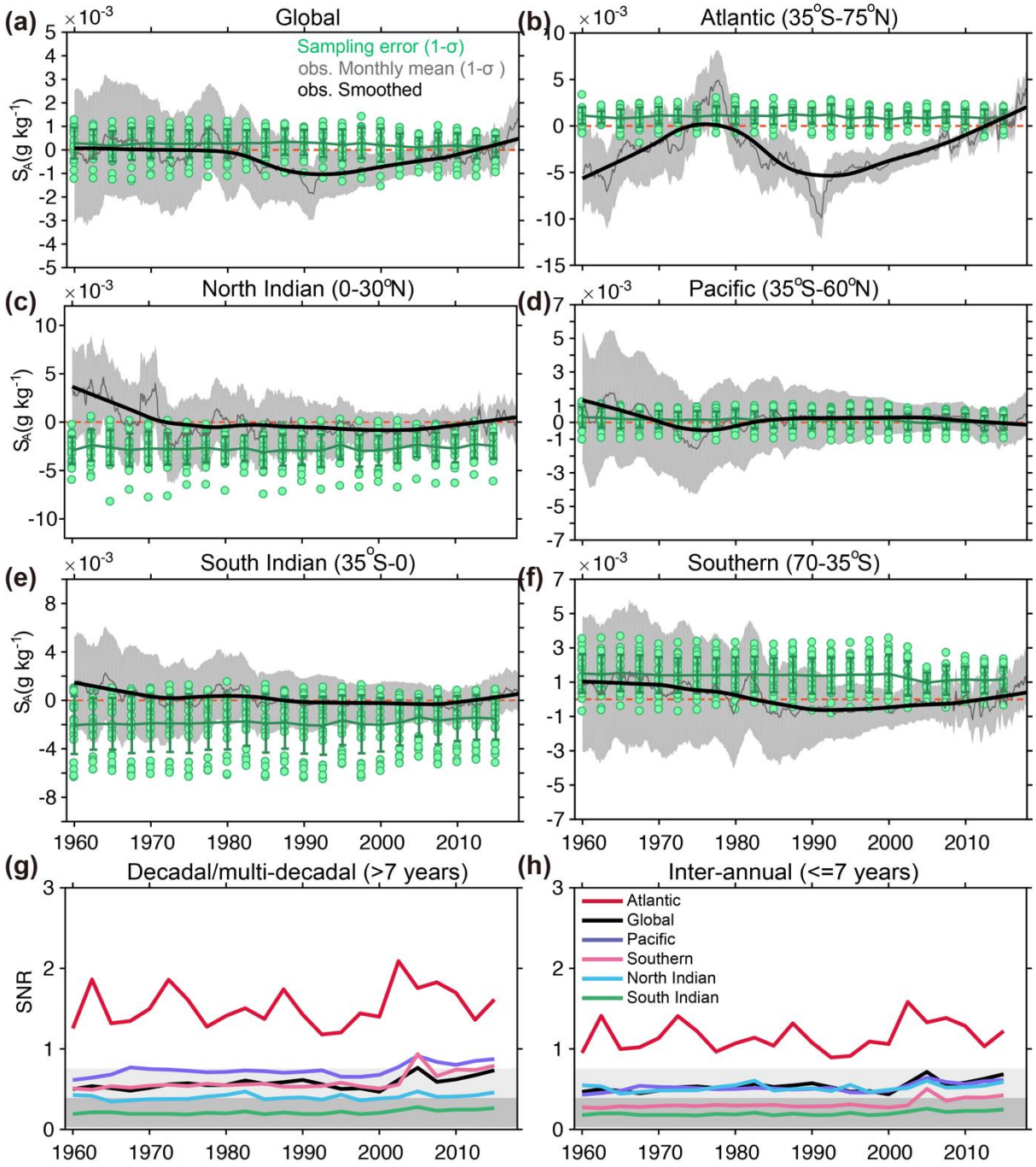

Supplementary Fig. S4. As for Fig. S2 but for 1000-1500m.

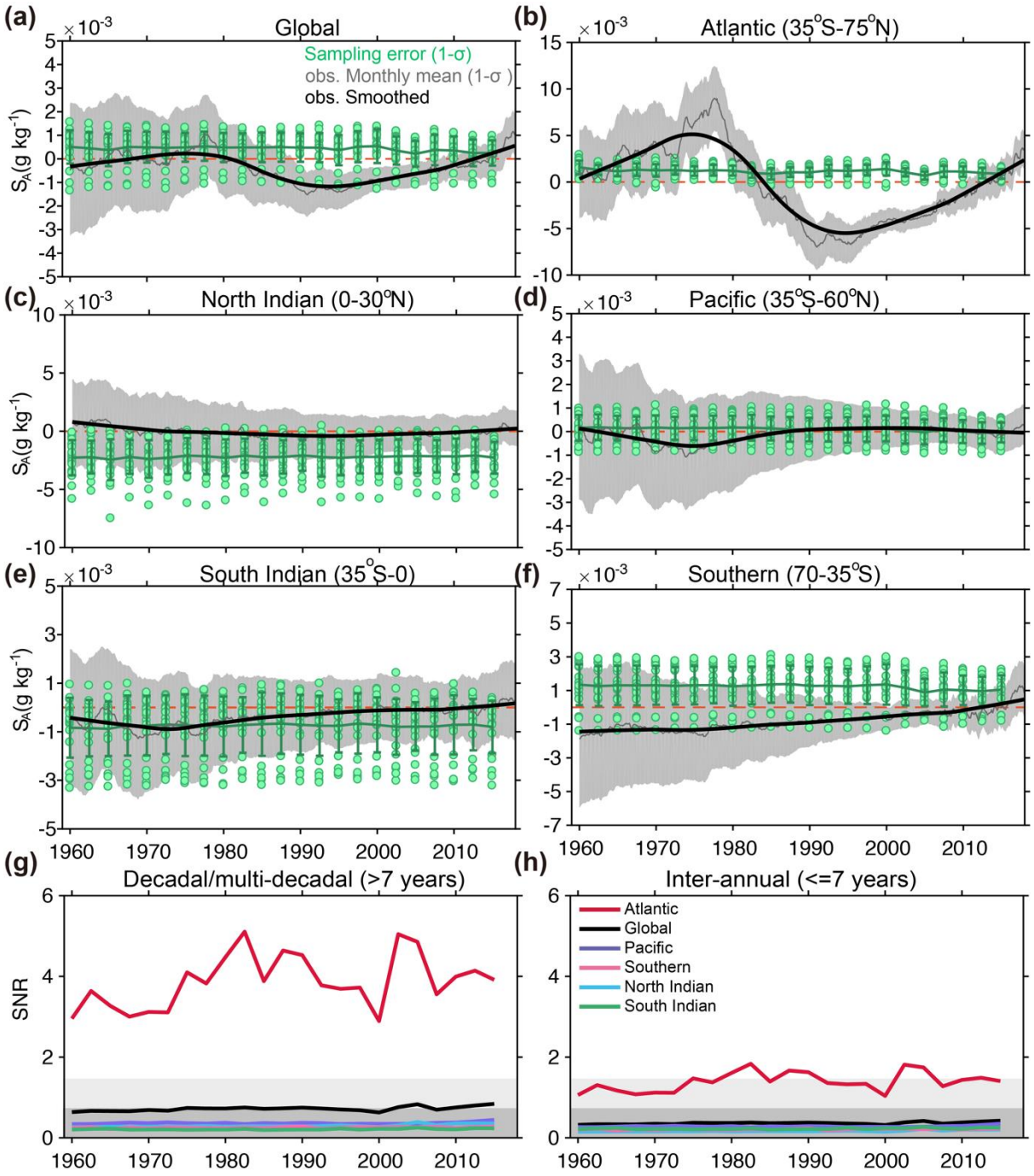

Supplementary Fig. S5. As for Fig. S2 but for 1500-2000m.

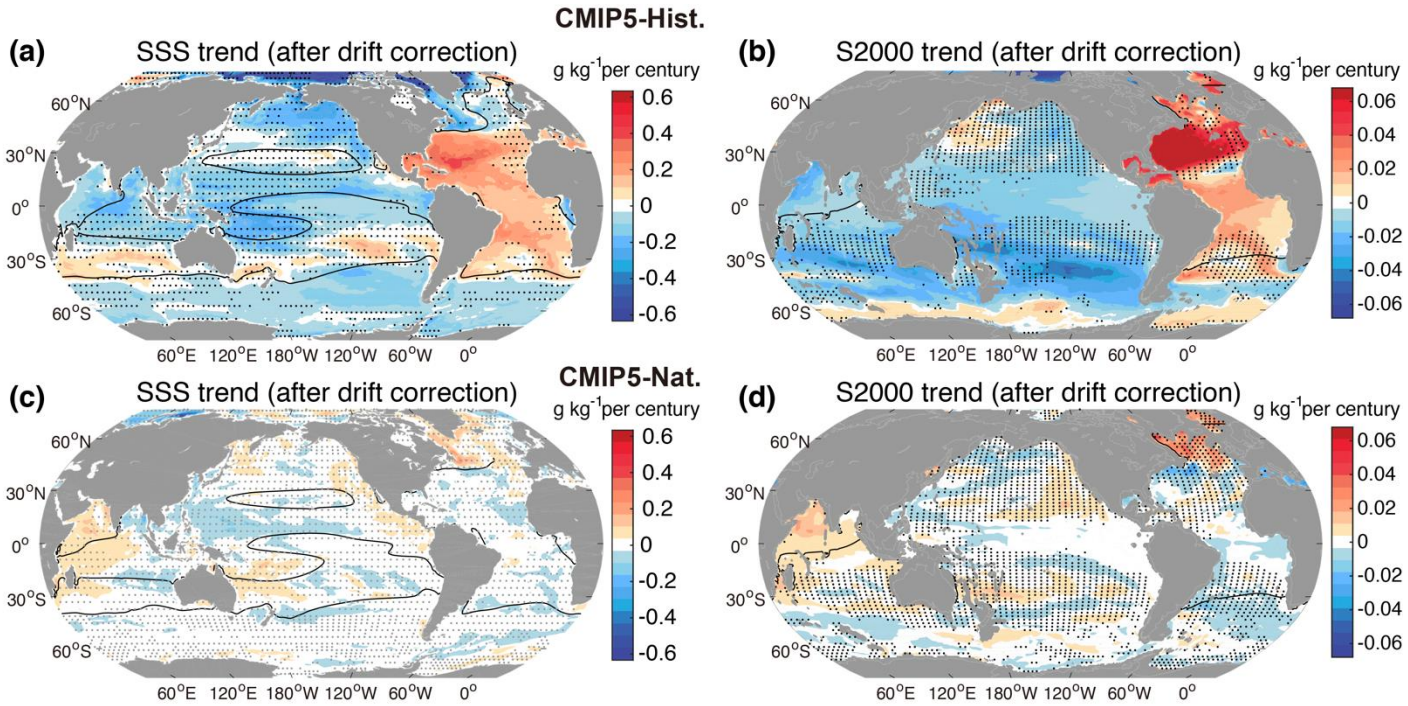

Supplementary Fig. S6. As for Fig. 13c, d, e, f but after drift corrections.

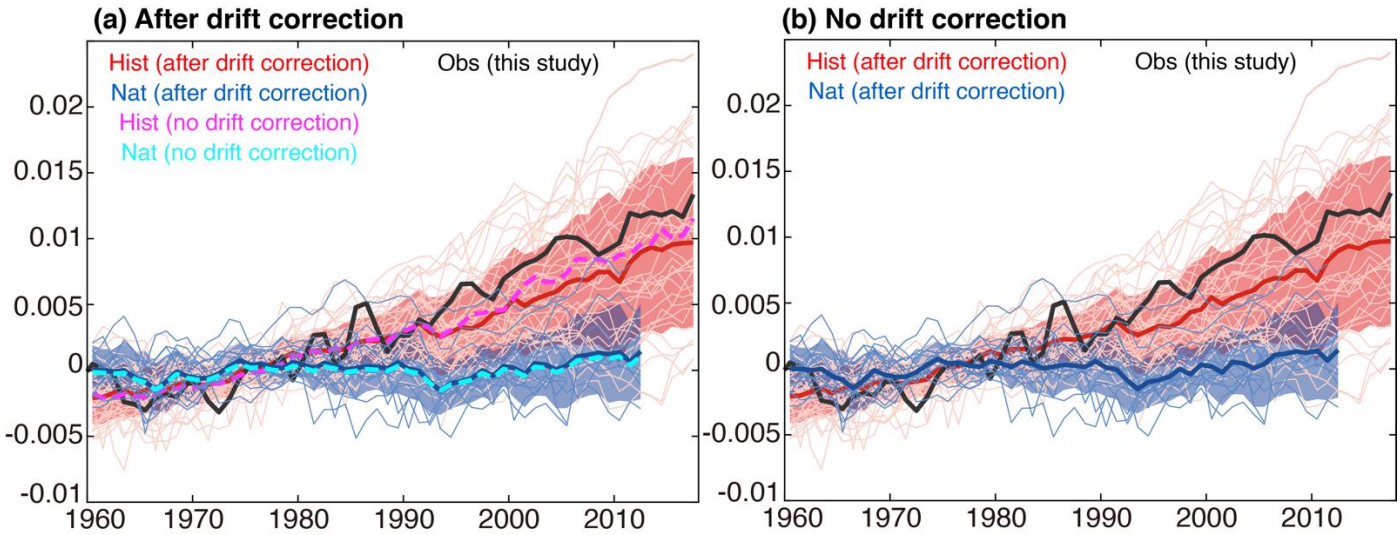

Supplementary Fig. S7. SC2000 calculated using models with (a) or without (b) model-drift correction. Panel-(b) is the same to Fig. 15a in the main manuscript. For comparison, in (a), the model ensemble median without drift correction are added in dashed lines for Hist (purple) and Nat (cyan). Observational estimate of annual mean SC2000 time series is in black from 1960 to 2017. The anomalies are relative to a 1960-1989 baseline.

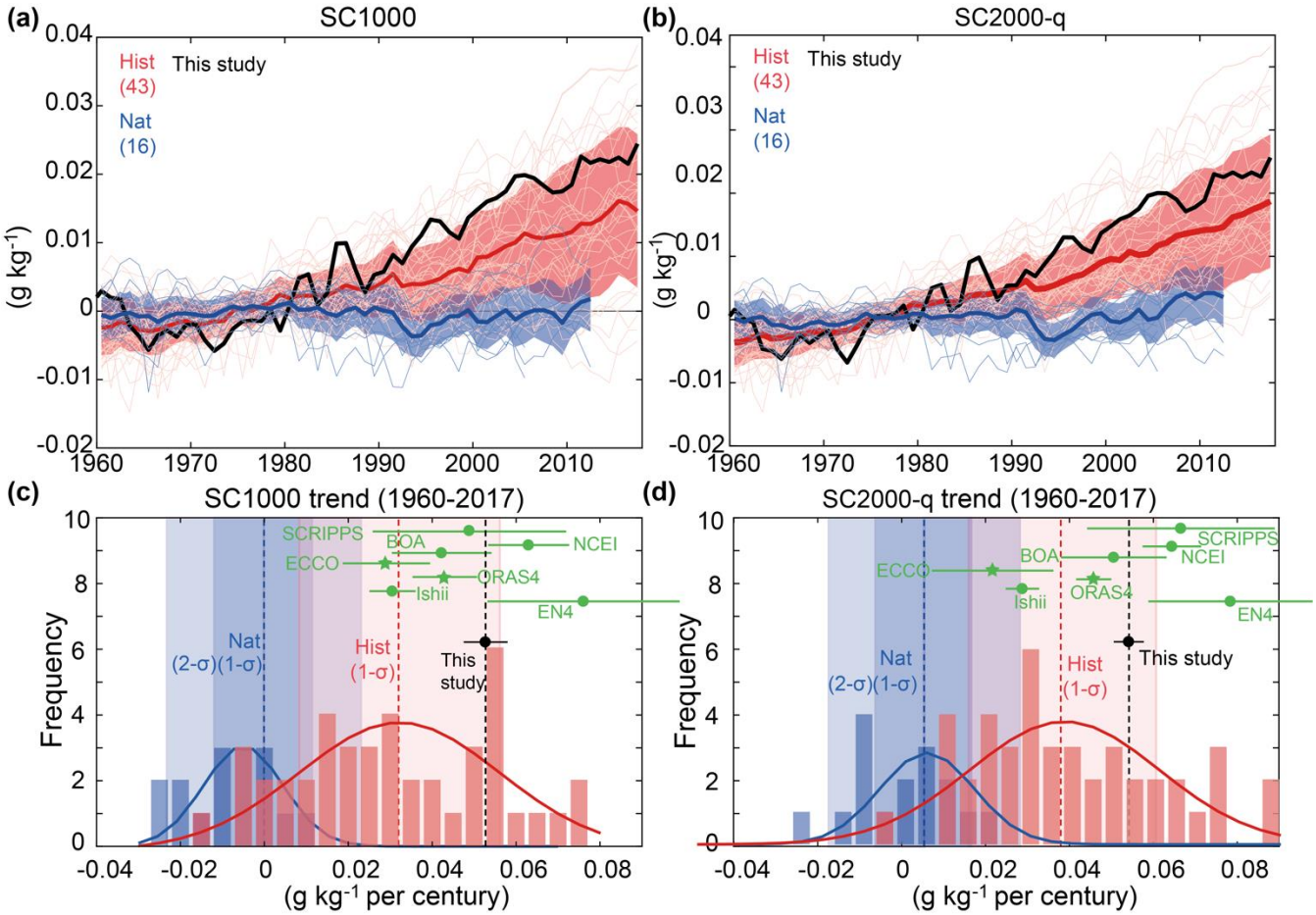

Supplementary Fig. S8. As for Fig. 15 but for SC1000 (a, c) and SC2000-q (b, d) changes.

Supplementary Table S1. A list of CMIP5 models and experiments analyzed in this study. The red texts denote the models that is used to defer E-P/S correlation, because all Hist and projections are available for both E-P and salinity in these models. Note "S" in the top column denotes the model availability for salinity for different experiments. There is only one "E-P" column because all the noted models have all experiments available. Only the first ensemble member is used (denoted as "R1").

	Model name	Modeling center	S Nat	S Hist	S RCP2.6	S RCP4.5	S RCP8.5	E-P
1	BCC_CSM1.1	Beijing Climate Center(BBC)	R1	R1	R1	R1	R1	R1
2	BCC_CSM1.1m	Beijing Climate Center(BBC)		R1	R1	R1	R1	R1
3	BNU_ESM	GCESS,BNU,Beijing,China				R1		
4	CanESM2	Canadian Center for Climate modeling and Analysis	R1	R1	R1	R1	R1	R1
5	CMCC_CESM	Centro Euro-Mediterraneo per i Cambiamenti Climatici, Bologna, Italy		R1		R1	R1	
6	CMCC_CM	Centro Euro-Mediterraneo per i Cambiamenti Climatici, Bologna, Italy		R1		R1		
7	CMCC_CMS	Centro Euro-Mediterraneo per i Cambiamenti Climatici, Bologna, Italy				R1	R1	
8	CNRM_CM5	Centre National de Recherches Meteorologiques,Toulouse		R1	R1	R1	R1	R1
9	ACCESS1-0	Commonwealth Scientific and Industrial Research Organisation		R1		R1	R1	
10	ACCESS1-3	Commonwealth Scientific and Industrial Research Organisation		R1		R1	R1	
11	CSIRO_Mk3-6-0	Australian Commonwealth Scientific and Industrial Research Organization	R1	R1	R1	R1	R1	R1
12	FIO_ESM	FIO(The First Institution of Oceanography,SOA,Qingdao,China)		R1	R1	R1	R1	R1
13	EC_EARTH	EC-Earth (European Earth System Model)		R1	R1	R1	R1	
14	IPSL_CM5A_LR	Institute Pierre Simon Laplace, Paris, France	R1	R1	R1	R1	R1	R1
15	IPSL_CM5A_MR	Institute Pierre Simon Laplace, Paris, France		R1	R1	R1	R1	R1
16	IPSL_CM5B_LR	Institute Pierre Simon Laplace, Paris, France		R1		R1		
17	FGOALS_g2	Institute of Atmospheric Physics, Chinese Academy of Sciences, Beijing	R1	R1	R1	R1	R1	R1

18	MIROC5	Atmosphere and Ocean Research Institute, The University of Tokyo,Japan		R1	R1	R1	R1	R1
19	MIROC_ESM_CHEM	JAMSTEC (Japan Agency for Marine-Earth Science and Technology, Kanagawa, Japan), AORI (Atmosphere and Ocean Research Institute, The University of Tokyo, Chiba, Japan)	R1	R1	R1	R1	R1	R1
20	HadCM3	Met Office Hadley Centre, Fitzroy Road, Exeter, Devon, EX1 3PB, UK				R1		
21	HadGEM2_CC	Met Office Hadley Centre, Fitzroy Road, Exeter, Devon, EX1 3PB, UK		R1		R1	R1	
22	HadGEM2_ES	Met Office Hadley Centre, Fitzroy Road, Exeter, Devon, EX1 3PB, UK		R1	R1	R1	R1	
23	MPI_ESM_LR	Max Planck Institute for Meteorology		R1	R1	R1	R1	R1
24	MPI_ESM_MR	Max Planck Institute for Meteorology		R1	R1	R1	R1	R1
25	MRI_CGCM3	Meteorological Research Institute, Tsukuba, Japan	R1	R1	R1	R1	R1	R1
26	CanCM4	Canadian Center for Climate modeling and Analysis		R1	R1	R1	R1	
27	GISS_E2_H	Goddard Institute for Space Studies, New York	R1	R1		R1		R1
28	GISS_E2_H_CC	Goddard Institute for Space Studies, New York		R1		R1	R1	
29	GISS_E2_R	Goddard Institute for Space Studies, New York	R1	R1	R1	R1	R1	R1
30	GISS_E2_R_CC	Goddard Institute for Space Studies, New York		R1		R1	R1	
31	NorESM1_M	Norwegian Climate Centre	R1	R1	R1	R1	R1	R1
32	NorESM1_ME	Norwegian Climate Centre		R1	R1	R1	R1	R1
33	CCSM4	NCAR (National Center for Atmospheric Research) Boulder, CO, USA	R1	R1	R1	R1	R1	R1
34	HadGEM2_AO	NIMR (National Institute of Meteorological Research, Seoul, South Korea)		R1	R1	R1	R1	
35	CESM1-BGC	NSF/DOE NCAR (National Center for Atmospheric Research) Boulder, CO, USA		R1		R1	R1	
36	CESM1_CAM5	NSF/DOE NCAR (National Center for Atmospheric Research) Boulder, CO, USA	R1	R1	R1	R1	R1	
37	GFDL_CM2p1	NOAA GFDL		R1		R1		
38	GFDL_CM3	NOAA GFDL	R1	R1	R1	R1	R1	R1
39	GFDL_ESM2G	NOAA GFDL		R1	R1	R1	R1	R1
40	GFDL-ESM2M	NOAA GFDL	R1	R1	R1	R1	R1	R1

41	MRI_ESM1	Meteorological Research Institute, Tsukuba, Japan		R1	R1			
42	CESM1_WACCM	NSF/DOE NCAR (National Center for Atmospheric Research) Boulder, CO, USA		R1	R1			
43	CESM1_FASTCHEM	NSF/DOE NCAR (National Center for Atmospheric Research) Boulder, CO, USA		R1	R1			
44	CESM1_CAM5_1_FV	NSF/DOE NCAR (National Center for Atmospheric Research) Boulder, CO, USA	R1	R1	R1			
45	MPI_ESM_P	Max Planck Institute for Meteorology		R1	R1			
46	CNRM_CM5_2	Centre National de Recherches Meteorologiques,Toulouse	R1	R1	R1			